

Intrinsic mid-IR chirality and chiral thermal emission from twisted bilayers

Michael T. Enders¹

Mitradeep Sarkar¹

Evgenia Klironomou¹

Michela Florinda Picardi¹

Aleksandra Deeva¹

Georgia T. Papadakis^{1,†}

¹ICFO — Institut de Ciències Fotoniques,
The Barcelona Institute of Science and Technology,
08860 Castelldefels (Barcelona), Spain

The ability to detect and engineer chirality plays a defining role in understanding nature, presenting itself in various phenomena ranging from the formation of DNA to enzymatic activities and digital encoding. Inducing a chiral response using nanophotonic practices typically entails lithographic efforts to create micro- and nano-structures that break mirror symmetry. Even with such configurations and despite the ubiquitousness of thermal radiation, generating chiral light at mid-infrared frequencies through thermal emission remains a challenge, since incandescence is by nature incoherent and unpolarized. In contrast to lithography-based approaches, we demonstrate that unpatterned twisted bilayers of in-plane anisotropic materials serve as a new material platform for intrinsic mid-infrared chirality engineering. Via absorption spectroscopy as well as direct thermal emission measurements, we report large circular dichroism and asymmetric circularly polarized thermal emission from exfoliated twisted bilayers of α -molybdenum trioxide (α -MoO₃). These findings highlight the potential of twisted layered van der Waals materials for polarization control and advanced thermal infrared technologies.

Introduction

Chirality, the property of a geometrical object that renders it non-super-imposable on its mirror image, plays a crucial role across various scientific disciplines. Ranging from the fundamental building blocks of life, such as 21 out of the 22 proteinogenic amino acids, to the intricate double-helix structure of DNA, chirality is ubiquitous [1]. The inherent “handedness” of chiral objects is particularly relevant in the functionalities and interactions of biological molecules, ranging from enzymatic activities to genetic encoding. In the realm of molecular and materials science, chirality significantly influences the optical and chemical properties of substances [2, 3].

The mid-IR region of the electromagnetic spectrum is particularly pertinent in studying chiral structures. This spectral region encompasses the fundamental vibrational modes of molecules, which are sensitive to chiral configurations [4], and this renders it particularly relevant to numerous applications. In pharmaceuticals, the differentiation of enantiomers – molecules that are mirror images of each other – is vital, as they can exhibit distinct biological activities and therapeutic

effects [5, 6]. Techniques such as vibrational circular dichroism spectroscopy exploit mid-IR light to distinguish between these enantiomers, providing critical insights into their absolute configurations and purity [7, 8]. Importantly, at room temperatures, the black-body spectrum of thermal radiation, representing the maximal emission extracted from macroscopic objects, peaks in the mid-IR region, specifically at wavelengths near 10 μm . This makes the mid-IR range particularly relevant for the aforementioned applications [9], by probing chiral properties of materials through incandescent light. It is noteworthy, however, that while thermal emission holds promise for cheap IR sources for such applications and others, light generated from incandescence is intrinsically achiral [10]. To address this limitation, significant lithographic efforts are necessary to introduce a chiral degree of freedom into thermal emission sources [11].

An object is chiral when it cannot be superimposed with its mirror image by means of any in-plane translation and rotation [12]. This requires the object to not possess inversion-rotation symmetry. A simple chiral shape in two-dimensions is an L-shape since, as shown in Fig. 1a, it cannot be superimposed onto its mirror image under rotation nor translation. Based on this shape,

[†]georgia.papadakis@icfo.eu

planar chiral metamaterials with similarly shaped unit cells have been demonstrated previously [13–23]. Since the chiral response of each individual unit cell remains small, these are often organized into a lattice to enhance the net chiral response. Alternatively, metamaterials composed of arrays of three-dimensional chiral structures, such as helices (Fig. 1b), can achieve circular dichroism (CD) values close to 1. In these materials, one handedness of light is almost entirely suppressed [24]. Recently, it has been shown that vertical stacking and twisting achiral metasurfaces can also yield a chiral response [25]. All aforementioned approaches, however, rely on significant high-resolution lithography in order to structurally induce broken symmetries, and generally require considerable light propagation within the meta-architecture in order to attain sufficiently large CD.

In this work, we introduce a fundamentally different approach to inducing chirality in three dimensions. Our approach eliminates the need for complex nanofabrication techniques for creating chiral architectures. Instead of relying on external structural modifications, our method leverages the intrinsic properties of materials to break inversion-rotation symmetry (see Fig. 1d) by stacking them in twisted bilayer configurations. Thus, the only requirement for inducing a chiral response in this platform is an intrinsic in-plane anisotropic material response. As we show via reflectivity and direct thermal emissivity measurements, this strategy allows for the generation of chiral light through the alignment of bilayers. Our results offer a simple and scalable solution to inducing and controlling chirality in the mid-IR range.

Results

Chiral objects interact differently with left- and right-circularly polarized light, which can be observed with CD absorption spectroscopy. This technique measures the difference in absorption between left- and right-circularly polarized light to detect chirality. CD can be measured not only in chiral samples but also in achiral samples when the combined system of the sample and the impinging light upon it breaks mirror symmetry, often termed *extrinsic* chirality. For example, when light strikes a planar structure lacking two-fold rotational symmetry at an oblique angle, the system can exhibit extrinsic chirality (Fig. 1c) and measurable CD, even if the material itself is achiral [26–29]. By contrast, as considered in this work, when *two* anisotropic layers are superimposed with a twist angle between them (Fig. 1d), mirror symmetry is broken even at normal incidence, altering how the bilayer system interacts with circularly polarized light. The resulting configuration exhibits *intrinsic* chirality, where the entire

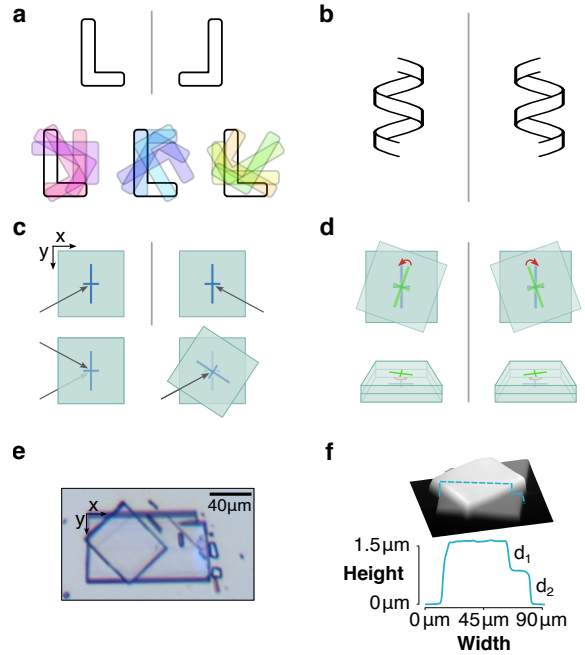


Fig. 1: **Chirality.** **a** L-shape and its mirror image. In the bottom part, the image is rotated, highlighting the impossibility of mapping it onto the original shape. **b** A helix and its mirror image as an example of a chiral structure in 3D. **c** Extrinsic chirality of light impinging onto an anisotropic medium at an oblique angle. **d** Two anisotropic materials stacked on top of each other, with misaligned crystal axes, breaking mirror symmetry. **e** Microscope image of a twisted bilayer α -MoO₃ sample (called *Device 2* in the following measurements. The x - and y -axes of the crystal are indicated for the bottom flake. **f** AFM scan of the height profile of the sample shown **e**. The lower plot shows the height profile along the blue line, where thickness d_1 refers to the top flake and d_2 to the bottom flake.

stack exhibits inherent handedness, since this twisting breaks the in-plane symmetry of each individual layer.

Several van der Waals materials, like α -MoO₃ [30–32] and α -vanadium pentoxide (α -V₂O₅) [33], have been recently identified to have a naturally occurring extreme in-plane anisotropy in the mid-IR [34–44]. Here, without loss of generality, we demonstrate the effect of an intrinsic chiral response using twisted anisotropic bilayers of α -MoO₃. Due to the orthorhombic structure of the α -MoO₃ crystal [32], exfoliated flakes typically possess a rectangular shape, as shown in Fig. 1e, where a microscope image of a twisted bilayer is shown. We refer to the crystal directions [100] and [001], as the x - and y -axis (indicated in Fig. 1e), respectively. The linear birefringence Δn and linear dichroism Δk of a single flake of α -MoO₃, defined as the difference in the refractive indices and extinction coefficients along the two in-plane crystal axes (x and y), are shown in

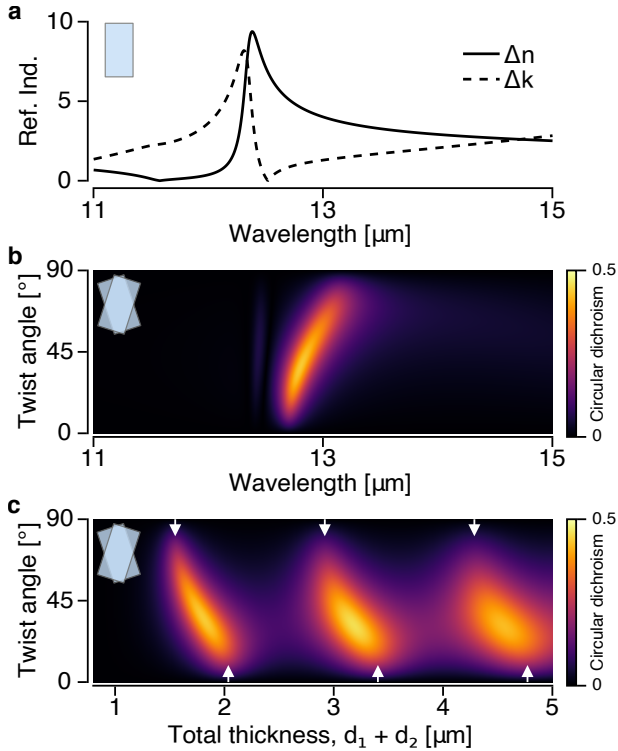


Fig. 2: **Molybdenum trioxide.** **a** Linear birefringence Δn and linear dichroism Δk of a single $\alpha\text{-MoO}_3$ flake. **b** Transfer matrix simulation of a twisted bilayer device composed of $\alpha\text{-MoO}_3$, with $d_1 = 0.8 \mu\text{m}$ and $d_2 = 1 \mu\text{m}$. Circular dichroism spectrum as a function of wavelength and relative twist angle between the two $\alpha\text{-MoO}_3$ layers. **c** Dependence of circular dichroism on d_2 , while $d_1 = 0.8 \mu\text{m}$ at a wavelength of $12.8 \mu\text{m}$. The x -axis shows the total thickness of the bilayer. White arrows indicate the total thickness for which the structure is resonant at twist angles of 0° (bottom ones) and 90° (top ones).

Fig. 2a. As shown, both Δn and Δk are resonant at the frequency corresponding to the phonon polariton resonance of $\alpha\text{-MoO}_3$ along the x -direction. Due to weak interlayer interactions, $\alpha\text{-MoO}_3$ is an excellent material to fabricate twisted stacks. An atomic force microscopy (AFM) scan of the twisted bilayer is presented in Fig. 1f, where the height profile of both flakes is displayed. Henceforth, the thicknesses of the top and bottom flakes are denoted as d_1 and d_2 , respectively.

Fig. 2b shows transfer matrix simulations of CD from a $\alpha\text{-MoO}_3$ twisted bilayer on top of gold substrate at normal incidence as a function of the relative twist angle between the flakes and wavelength. For a twist angle of approximately 36° , $\text{CD} = 0.44$, with $d_1 = 0.8 \mu\text{m}$ and $d_2 = 1 \mu\text{m}$. As explained above, this effect originates from the broken mirror symmetry upon twisting the two bilayers with respect to each other, which induces chirality. As expected, at a twist angle of 0° and 90° ,

$\text{CD} = 0$, since mirror symmetry is preserved in both cases (see Fig. 1d). Although mere twisting of the layers ensures broken mirror symmetry, the effect is enhanced via interference, by inducing Fabry–Pérot resonances within the bilayer via tuning the respective thicknesses of the two bilayers. This is shown in Fig. 2c, where the top layer’s thickness d_1 is kept constant at $1 \mu\text{m}$, while d_2 varies. The x -axis represents the total thickness of the bilayer, $d_1 + d_2$. At a twist angle of 0° – corresponding to a uniform crystal of $\alpha\text{-MoO}_3$ – the white arrows mark the total thickness at which the structure becomes resonant. The same applies to the white arrows at a twist angle of 90° , where the x -axis of the top layer of $\alpha\text{-MoO}_3$ aligns with the y -axis of the bottom layer. In both cases, CD vanishes, as mirror symmetry is preserved. Importantly, maximum CD occurs precisely at thicknesses between these two resonances. This observation allows selecting the operating wavelength and controlling its dependence on the twist angle.

As shown in the numerical results of Fig. 2, twisted bilayer $\alpha\text{-MoO}_3$ offers a significant advantage over traditional chiral meta-devices and related architectures [13–25] by eliminating the need for high-resolution lithography and complex fabrication processes. While several numerical studies have recently explored twisting layers of $\alpha\text{-MoO}_3$ and other materials for mid-IR and terahertz chirality [45–49], no experimental result has been reported previously. In this paper, we experimentally demonstrate large values of CD, which can be tuned by varying the twist angle and thickness of the two layers. Due to the extreme anisotropy of $\alpha\text{-MoO}_3$, the total thickness required for achieving large CD values remains deeply sub-wavelength. The strong CD is not only demonstrated with absorption spectroscopy, but also via direct thermal emission measurements, showcasing the potential of twisted bilayer $\alpha\text{-MoO}_3$ as a platform for designing thermal sources of chiral emission in the mid-IR.

We mechanically exfoliated flakes of $\alpha\text{-MoO}_3$ with polydimethylsiloxane-based exfoliation and transfer (X0 retention, DGL type from Gelpak) at 90°C [50]. Firstly, the bottom flake was transferred onto gold-coated (150nm) glass and consequently the top flake was transferred onto the bottom flake at the desired twist angle, using an optical microscope which enables rotation and positioning of the flakes. The dielectric permittivity of the batch of $\alpha\text{-MoO}_3$ (2D Semiconductors, Bridgman growth technique) used in the devices presented in this article was extracted using FTIR spectroscopy, following the method described in [51]. These permittivity values serve as the basis for our transfer matrix simulations and Fig. 2. To measure CD, we used an FTIR microscope in reflection mode, and inserted a polarizer and a waveplate in the beam path

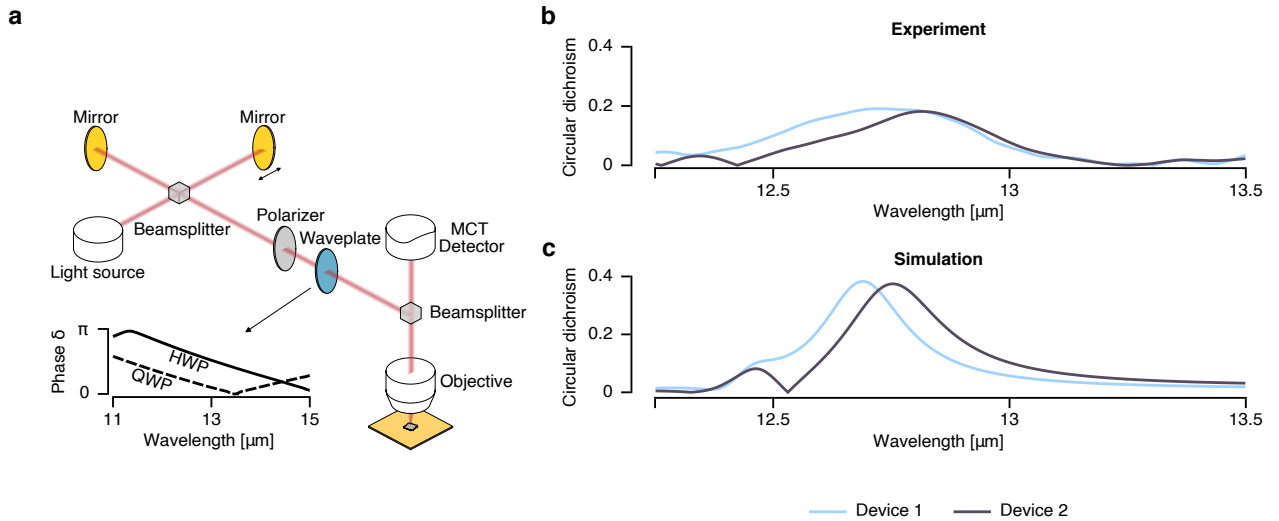


Fig. 3: Measurements of circular dichroism in reflection. **a** Schematic of the beam path of the FTIR microscope in reflection mode. The global light source emits unpolarized light, which is polarized using a linear polarizer and a waveplate, after passing through the interferometer. The light, now with known ellipticity, is focused on the sample and recollected with a $36\times$ reflective (Cassegrain) objective. A beamsplitter positioned before the objective directs the recollected beam to an MCT photodetector. **b** FTIR microscope measurements of the CD spectrum of two twisted bilayer α - MoO_3 devices (*Device 1* with $d_1 = 0.6 \mu\text{m}$, $d_2 = 1.1 \mu\text{m}$ and twist angle of 33° , *Device 2* with $d_1 = 0.85 \mu\text{m}$, $d_2 = 0.8 \mu\text{m}$ and twist angle of 42°). **c** Corresponding transfer matrix simulations for the two experimentally measured devices.

between the FTIR spectrometer and the microscope (see Fig. 3a).

We define CD in reflection mode as:

$$\text{CD}_{\text{ref}} = |R_{\circlearrowleft} - R_{\circlearrowright}|, \quad (1)$$

where $R_{\circlearrowleft/\circlearrowright}$ denote the reflectance of right/left-hand circularly polarized light. Due to the lack of available broadband quarter-wave plates in the mid-IR, we could not directly measure the reflectance of circularly polarized light. To solve this problem, we used a narrowband waveplate that is transparent in the spectral region of interest and introduces a known phase δ between the x - and y -component of the electromagnetic field. This way, we measured the reflected intensities R_{45° and R_{-45° , where linearly polarized light impinges on the waveplate oriented at 45° and -45° with respect to its crystal axis. It can be shown (see Supplementary Material) that:

$$\text{CD}_{\text{ref}} = \left| \frac{R_{45^\circ} - R_{-45^\circ}}{\sin(\delta)} \right|. \quad (2)$$

We conducted the measurements using two different narrowband waveplates, intentionally omitting operation near $\delta = 0$. In this way, the spectral range of each measurement was only limited by the transparency of the considered waveplate. We characterized the phase δ introduced by the two waveplates: a quarter-wave

plate and a half-wave plate with operational wavelength $11.3 \mu\text{m}$ (CdSe from VM-TIM GmbH), following the technique presented in [52] (see inset in Fig. 3). To minimize the error introduced by the conversion shown in Eq. 2, we chose the measurement of the waveplate where the factor $1/\sin(\delta)$ is smaller. This way, over the entire spectral region presented, this factor never exceeded 1.81 (see Supplementary Material).

The two twisted bilayer α - MoO_3 devices presented in this work have twisted areas with lateral dimensions ranging from $10 \mu\text{m}$ to $40 \mu\text{m}$. *Device 1* consists of a $0.6 \mu\text{m}$ thick flake on top of a $1.1 \mu\text{m}$ flake twisted at an angle of 33° . *Device 2* comprises a $0.8 \mu\text{m}$ flake on top of a $0.85 \mu\text{m}$ flake, twisted at an angle of 42° . Both devices are transferred onto a gold-coated glass substrate to perform CD measurements in reflection. Fig. 3b shows FTIR measurements of CD_{ref} defined in Eq. 1, for the two devices. We restrict our measurement to the twisted area of the devices using the knife-edge aperture of the FTIR microscope. Transfer matrix simulations of CD_{ref} of the same devices are shown in panel Fig. 3c.

In both devices, the measured CD_{ref} has a maximum value of nearly 0.2. Whilst the simulated CD_{ref} is considerably larger, the spectral position of maximum CD perfectly matches between simulation and experiment. The smaller value in the experimentally measured CD is

due to the small lateral dimensions of the twisted areas, which are in the order of magnitude of the measured wavelength. Since transfer matrix simulations work assuming plane surfaces with infinite lateral dimensions, edge effects that might appear are not considered. The values of measured CD are significant and demonstrate that mechanical twisting of anisotropic bi-layers can indeed induce a strong chiral effective response without any need for lithography. Below, we demonstrate that this chiral response can manifest itself in thermal emission measurements, thus significantly altering the incoherent characteristics of blackbody radiation. According to Kirchhoff's law of thermal radiation [53], the circular dichroism observed in the absorption properties of twisted bilayer α -MoO₃ should similarly present itself in a direct thermal emission experiment, leading to preferential emission of one circular polarization over the other. This is indeed demonstrated below.

We describe the polarization state of the emitted light by the Stokes parameters that contain all information regarding the correlation between orthogonal components of the electric field of light. For elliptically polarized light, the tip of the electric field vector traces an ellipse, as shown in Fig. 4. The polarization ellipse is defined in Cartesian coordinates in terms of the x and y components of the electric field vector ($E_{0,x}$ and $E_{0,y}$) by the orientation angle $0 \leq \psi \leq \pi$ and the ellipticity angle $-\pi/4 \leq \chi \leq \pi/4$. The polarization ellipse yields the following equation, $p^2 S_0^2 = S_1^2 + S_2^2 + S_3^2$, where:

$$\begin{aligned} S_0 &= E_{0,x}^2 + E_{0,y}^2 = I_0 \\ S_1 &= E_{0,x}^2 - E_{0,y}^2 = I_p \cos(2\chi) \cos(2\psi) \\ S_2 &= 2E_{0,x}E_{0,y} \cos(\delta) = I_p \cos(2\chi) \sin(2\psi) \\ S_3 &= 2E_{0,x}E_{0,y} \sin(\delta) = I_p \sin(2\chi). \end{aligned} \quad (3)$$

Here $S(\lambda) = [S_0(\lambda), S_1(\lambda), S_2(\lambda), S_3(\lambda)]$ represent the components of Stokes vector, and I_0 is the total intensity of light. The parameter p represents the degree of polarization, and when no depolarization is considered, $p = 1$, $I_0 = I_p$. The parameter S_0 represents the time-averaged intensity in the direction of propagation. Parameters S_1 and S_2 correspond to the difference of the intensities of the linearly polarized fields along the x and y directions and along 45° and -45° with respect to x -axis, respectively. S_3 denotes the difference between the intensities of right and left-hand circularly polarized light. Hence, by definition (Eq. 1), S_3 represents the CD in emission (CD_{em}).

We characterized the polarization state of the emitted radiation from twisted bilayer α -MoO₃, using Stokes polarimetry (see Supplementary Material), by combining a linear polarizer and a half-wave plate, as described in Nguyen *et al.* [11] and Sabatke *et al.* [54]. We consider five independent sets of the polarizer and waveplate

orientations to retrieve the Stokes parameters. The half-waveplate enabled retrieving the Stokes parameters between $12 \mu\text{m}$ and $13.5 \mu\text{m}$. Additionally, the Stokes parameters were also calculated by transfer matrix simulations. The presented results correspond to absorptivity calculations $A = 1 - R$. In particular, the Stokes parameters were obtained as:

$$\begin{aligned} S_0 &= A_{\leftrightarrow}(\Phi = 0^\circ) + A_{\updownarrow}(\Phi = 0^\circ), \\ S_1 &= A_{\leftrightarrow}(\Phi = 0^\circ) - A_{\updownarrow}(\Phi = 0^\circ), \\ S_2 &= A_{\leftrightarrow}(\Phi = 45^\circ) - A_{\updownarrow}(\Phi = 45^\circ). \\ S_3 &= A_{\circ} - A_{\ominus}. \end{aligned} \quad (4)$$

Fig. 4 shows the experimentally retrieved and theoretically predicted Stokes parameters, normalized by S_0 . As shown, S_2 and S_3 have a fair agreement between the measured and simulated spectra. In particular, the Stokes parameter $S_3 = CD_{em} = CD_{ref}$. This is evident from the measured S_3 shown in Fig. 4 and the CD_{ref} shown in Fig. 3 (*Device 2*). Similar to CD_{ref} , the measured S_3 reaches 0.2 and is approximately half of that expected from the simulations. The same reasons as discussed in relation to Fig. 3 are responsible for this discrepancy. The parameter S_1 is sensitive to the orientation of the sample, the polarizer and the waveplate, making its retrieval least precise. In particular, direct emissivity measurements are limited by the small thermal emission from α -MoO₃ at the measured temperature (573 K). At this temperature, which is not considerably higher than room-temperature, the emitted signal from the sample is comparable in magnitude to the background thermal emission arising from the instrument itself, increasing the uncertainty related to the evaluation of the Stokes parameters.

We have characterized the polarization state of the light emitted from the device due to incandescence. We note that, at the wavelength for which S_3 is maximized ($\lambda = 12.8 \mu\text{m}$), the degree of polarization p measured for the device is $p = 0.24$, which suggests that the emitted light is considerably depolarized. However, the non-zero values of S_3 in the same wavelength range confirm the chiro-optical characteristics of the twisted flakes. We show the polarization ellipse for the polarized part of the emitted light in Fig. 4c and e, corresponding to measurements and calculations. As shown, at $\lambda = 12.8 \mu\text{m}$, the dominant component is right-handed elliptically polarized, thus validating the chirality of the twisted flakes.

Discussion

We successfully fabricated twisted bilayer α -MoO₃ devices that exhibit intrinsic chirality. The fabricated devices do not require complex nanofabrication techniques and are deeply sub-wavelength. We experimen-

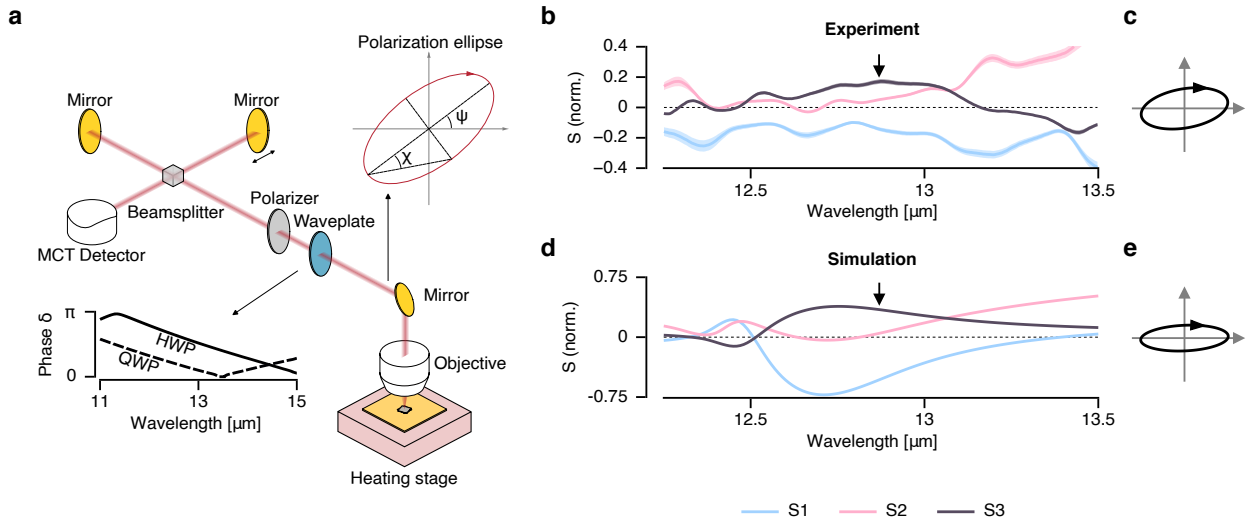


Fig. 4: **Circular dichroism in emission.** **a** Schematic of the beam path of the FTIR microscope in emission mode. The sample is placed on top of a heating stage and the emitted radiation is collected by $36\times$ reflective (Cassegrain) objective. After passing through a wave plate and polarizer the light enters the interferometer and is measured by an MCT detector afterwards. **b** Measured normalized Stokes parameters. The black arrow indicates the wavelength at which the polarization ellipse in **c** is shown. **d** Transfer matrix simulations of normalized Stokes parameters and corresponding polarization ellipse in **e**.

tally demonstrated significantly large values of CD via absorption measurements, providing new insights into the optical properties and potential avenues of twisted bilayer systems. Importantly, in addition to absorption measurements at room temperatures, we directly measured the thermal emission from these structures and observed circularly polarized thermal emission, further validating their chiral nature.

Notably, the thermal emission measurements were performed at a relatively low temperature of 573 K. Despite challenges related to conducting thermal emissivity measurements at low-temperatures, such as the low-emission signal from devices that do not surpass few tens of microns in lateral dimensions (see Fig. 1e and f), we were able to detect and confirm the circular polarization state of the emitted light. This highlights the robustness of twisted bilayer devices and their potential for applications in chiral and infrared photonics that leverage thermal radiation.

We hope that our findings open new avenues in the exploration of twisted bilayer systems that go beyond transport measurements and related exotic physics [35, 37, 55–57] and into the physics of thermal radiation and far-field nanophotonics. These results lay the groundwork for developing infrared optical devices for light emission and polarization control in a simple, planar, and scalable platform.

Acknowledgments We acknowledge fruitful discussion with Riccardo Bertini, Krystian Nowakowski,

and Prof. Frank Koppens in the Quantum Nano-Optoelectronics Group at ICFO and the generous sharing of optical components. We also acknowledge initial discussions with Dr. Ivan Fernandez Gorbato (Karlsruhe institute of Technology). MTE acknowledges financial support from MCIN/AEI/10.13039/501100011033 (PRE2020-094401) and FSE “El FSE invierte en tu futuro”. MFP Acknowledges support from the Optica Foundation 20th Anniversary Challenge Award. MFP and GTP received the support of fellowships from “la Caixa” Foundation (ID 100010434). The fellowship codes are LCF/BQ/PI23/11970026 and LCF/BQ/PI21/11830019. GTP also acknowledges support from the Spanish MICINN (PID2021-125441OA-I00, PID2020-112625GB-I00, and CEX2019-000910-S), Generalitat de Catalunya (2021 SGR 01443), Fundació Cellex, and Fundació Mir-Puig.

References

1. Meierhenrich, U. *Amino Acids and the Asymmetry of Life: Caught in the Act of Formation* 1st ed. 242 pp. (Springer Berlin Heidelberg, 2008).
2. Collins, J. T., Kuppe, C., Hooper, D. C., Sibilia, C., Centini, M. & Valev, V. K. Chirality and Chiroptical Effects in Metal Nanostructures: Fundamentals and Current Trends. *Advanced Op-*

- tical Materials* **5**, 1700182. doi:10.1002/adom.201700182 (2017).
3. Hentschel, M., Schäferling, M., Duan, X., Giessen, H. & Liu, N. Chiral Plasmonics. *Science Advances* **3**, e1602735. doi:10.1126/sciadv.1602735 (2017).
 4. Nafie, L. A. *Vibrational Optical Activity: Principles and Applications* 1st ed. doi:10.1002/9781119976516 (Wiley, 2011).
 5. *Chirality in Drug Design and Development* (eds Reddy, I. K. & Mehvar, R.) 444 pp. (Dekker, New York, NY, 2004).
 6. Smith, S. W. Chiral Toxicology: It's the Same Thing... Only Different. *Toxicological Sciences* **110**, 4–30. doi:10.1093/toxsci/kfp097 (2009).
 7. Jähnigen, S. Vibrational Circular Dichroism Spectroscopy of Chiral Molecular Crystals: Insights from Theory. *Angewandte Chemie International Edition* **62**, e202303595. doi:10.1002/anie.202303595 (2023).
 8. Xu, C., Ren, Z., Zhou, H., Zhou, J., Ho, C. P., Wang, N. & Lee, C. Expanding Chiral Metamaterials for Retrieving Fingerprints via Vibrational Circular Dichroism. *Light: Science & Applications* **12**, 154. doi:10.1038/s41377-023-01186-3 (2023).
 9. Baranov, D. G., Xiao, Y., Nechepurenko, I. A., Krasnok, A., Alù, A. & Kats, M. A. Nanophotonic Engineering of Far-Field Thermal Emitters. *Nature Materials* **18**, 920–930. doi:10.1038/s41563-019-0363-y (2019).
 10. Greffet, J.-J., Carminati, R., Joulain, K., Mulet, J.-P., Mainguy, S. & Chen, Y. Coherent Emission of Light by Thermal Sources. *Nature* **416**, 61–64. doi:10.1038/416061a (2002).
 11. Nguyen, A., Hugonin, J.-P., Coutrot, A.-L., Garcia-Caurel, E., Vest, B. & Greffet, J.-J. Large Circular Dichroism in the Emission from an Incandescent Metasurface. *Optica* **10**, 232–238. doi:10.1364/OPTICA.480292 (2023).
 12. Petitjean, M. Chirality in metric spaces. en. *Optimization Letters* **14**, 329–338. doi:10.1007/s11590-017-1189-7 (2020).
 13. Arteaga, O., Sancho-Parramon, J., Nichols, S., Maoz, B. M., Canillas, A., Bosch, S., Markovich, G. & Kahr, B. Relation between 2D/3D Chirality and the Appearance of Chiroptical Effects in Real Nanostructures. *Optics Express* **24**, 2242–2252. doi:10.1364/OE.24.002242 (2016).
 14. Bai, B., Svirko, Y., Turunen, J. & Vallius, T. Optical Activity in Planar Chiral Metamaterials: Theoretical Study. *Physical Review A* **76**, 023811. doi:10.1103/PhysRevA.76.023811 (2007).
 15. Decker, M., Klein, M. W., Wegener, M. & Linden, S. Circular Dichroism of Planar Chiral Magnetic Metamaterials. *Optics Letters* **32**, 856–858. doi:10.1364/OL.32.000856 (2007).
 16. Hopkins, B., Poddubny, A. N., Miroshnichenko, A. E. & Kivshar, Y. S. Circular Dichroism Induced by Fano Resonances in Planar Chiral Oligomers. *Laser & Photonics Reviews* **10**, 137–146. doi:10.1002/lpor.201500222 (2016).
 17. Kuwata-Gonokami, M., Saito, N., Ino, Y., Kauranen, M., Jefimovs, K., Vallius, T., Turunen, J. & Svirko, Y. Giant Optical Activity in Quasi-Two-Dimensional Planar Nanostructures. *Physical Review Letters* **95**, 227401. doi:10.1103/PhysRevLett.95.227401 (2005).
 18. Narushima, T., Hashiyada, S. & Okamoto, H. Optical Activity Governed by Local Chiral Structures in Two-Dimensional Curved Metallic Nanostructures. *Chirality* **28**, 540–544. doi:10.1002/chir.22611 (2016).
 19. Narushima, T. & Okamoto, H. Circular Dichroism Nano-Imaging of Two-Dimensional Chiral Metal Nanostructures. *Physical Chemistry Chemical Physics* **15**, 13805–13809. doi:10.1039/C3CP50854D (2013).
 20. Narushima, T. & Okamoto, H. Strong Nanoscale Optical Activity Localized in Two-Dimensional Chiral Metal Nanostructures. *The Journal of Physical Chemistry C* **117**, 23964–23969. doi:10.1021/jp409072h (2013).
 21. Shi, T., Deng, Z.-L., Geng, G., Zeng, X., Zeng, Y., Hu, G., Overvig, A., Li, J., Qiu, C.-W., Alù, A., Kivshar, Y. S. & Li, X. Planar Chiral Metasurfaces with Maximal and Tunable Chiroptical Response Driven by Bound States in the Continuum. *Nature Communications* **13**, 4111. doi:10.1038/s41467-022-31877-1 (2022).
 22. Wu, S., Zhang, Z., Zhang, Y., Zhang, K., Zhou, L., Zhang, X. & Zhu, Y. Enhanced Rotation of the Polarization of a Light Beam Transmitted through a Silver Film with an Array of Perforated SSS-Shaped Holes. *Physical Review Letters* **110**, 207401. doi:10.1103/PhysRevLett.110.207401 (2013).
 23. Zu, S., Bao, Y. & Fang, Z. Planar Plasmonic Chiral Nanostructures. *Nanoscale* **8**, 3900–3905. doi:10.1039/C5NR09302C (2016).
 24. Gansel, J. K., Thiel, M., Rill, M. S., Decker, M., Bade, K., Saile, V., von Freymann, G., Linden, S. & Wegener, M. Gold Helix Photonic Metamaterial as Broadband Circular Polarizer. *Science* **325**, 1513–1515. doi:10.1126/science.1177031 (2009).

25. Zhao, Y., Belkin, M. A. & Alù, A. Twisted Optical Metamaterials for Planarized Ultrathin Broadband Circular Polarizers. *Nature Communications* **3**, 870. doi:10.1038/ncomms1877 (2012).
26. Verbiest, T., Kauranen, M., Van Rompaey, Y. & Persoons, A. Optical Activity of Anisotropic Achiral Surfaces. *Physical Review Letters* **77**, 1456–1459. doi:10.1103/PhysRevLett.77.1456 (1996).
27. Plum, E., Fedotov, V. A. & Zheludev, N. I. Optical Activity in Extrinsic Chiral Metamaterial. *Applied Physics Letters* **93**, 191911. doi:10.1063/1.3021082 (2008).
28. Plum, E., Liu, X.-X., Fedotov, V. A., Chen, Y., Tsai, D. P. & Zheludev, N. I. Metamaterials: Optical Activity without Chirality. *Physical Review Letters* **102**, 113902. doi:10.1103/PhysRevLett.102.113902 (2009).
29. Wu, B., Wang, M., Wu, F. & Wu, X. Strong Extrinsic Chirality in Biaxial Hyperbolic Material α -MoO₃ with in-Plane Anisotropy. *Applied Optics* **60**, 4599–4605. doi:10.1364/AO.426098 (2021).
30. Ma, W., Alonso-González, P., Li, S., Nikitin, A. Y., Yuan, J., Martín-Sánchez, J., Taboada-Gutiérrez, J., Amenabar, I., Li, P., Vélez, S., Tolland, C., Dai, Z., Zhang, Y., Sriram, S., Kalantar-Zadeh, K., Lee, S.-T., Hillenbrand, R. & Bao, Q. In-Plane Anisotropic and Ultra-Low-Loss Polaritons in a Natural van Der Waals Crystal. *Nature* **562**, 557–562. doi:10.1038/s41586-018-0618-9 (2018).
31. Zheng, Z., Chen, J., Wang, Y., Wang, X., Chen, X., Liu, P., Xu, J., Xie, W., Chen, H., Deng, S. & Xu, N. Highly Confined and Tunable Hyperbolic Phonon Polaritons in Van Der Waals Semiconducting Transition Metal Oxides. *Advanced Materials* **30**, 1705318. doi:10.1002/adma.201705318 (2018).
32. Álvarez-Pérez, G., Folland, T. G., Errea, I., Taboada-Gutiérrez, J., Duan, J., Martín-Sánchez, J., Tresguerres-Mata, A. I. F., Matson, J. R., Bylinkin, A., He, M., Ma, W., Bao, Q., Martín, J. I., Caldwell, J. D., Nikitin, A. Y. & Alonso-González, P. Infrared Permittivity of the Biaxial van Der Waals Semiconductor α -MoO₃ from Near- and Far-Field Correlative Studies. *Advanced Materials* **32**, 1908176. doi:10.1002/adma.201908176 (2020).
33. Taboada-Gutiérrez, J., Álvarez-Pérez, G., Duan, J., Ma, W., Crowley, K., Prieto, I., Bylinkin, A., Autore, M., Volkova, H., Kimura, K., Kimura, T., Berger, M.-H., Li, S., Bao, Q., Gao, X. P. A., Errea, I., Nikitin, A. Y., Hillenbrand, R., Martín-Sánchez, J. & Alonso-González, P. Broad Spectral Tuning of Ultra-Low-Loss Polaritons in a van Der Waals Crystal by Intercalation. *Nature Materials* **19**, 964–968. doi:10.1038/s41563-020-0665-0 (2020).
34. Abedini Dereshgi, S., Folland, T. G., Murthy, A. A., Song, X., Tanriover, I., Dravid, V. P., Caldwell, J. D. & Aydin, K. Lithography-Free IR Polarization Converters via Orthogonal in-Plane Phonons in α -MoO₃ Flakes. *Nature Communications* **11**, 9. doi:10.1038/s41467-020-19499-x (2020).
35. Chen, M., Lin, X., Dinh, T. H., Zheng, Z., Shen, J., Ma, Q., Chen, H., Jarillo-Herrero, P. & Dai, S. Configurable Phonon Polaritons in Twisted α -MoO₃. *Nature Materials* **19**, 1307–1311. doi:10.1038/s41563-020-0732-6 (2020).
36. Dai, Z., Hu, G., Si, G., Ou, Q., Zhang, Q., Balendhran, S., Rahman, F., Zhang, B. Y., Ou, J. Z., Li, G., Alù, A., Qiu, C.-W. & Bao, Q. Edge-Oriented and Steerable Hyperbolic Polaritons in Anisotropic van Der Waals Nanocavities. *Nature Communications* **11**, 6086. doi:10.1038/s41467-020-19913-4 (1 2020).
37. Hu, G., Ou, Q., Si, G., Wu, Y., Wu, J., Dai, Z., Krasnok, A., Mazor, Y., Zhang, Q., Bao, Q., Qiu, C.-W. & Alù, A. Topological Polaritons and Photonic Magic Angles in Twisted α -MoO₃ Bilayers. *Nature* **582**, 209–213. doi:10.1038/s41586-020-2359-9 (7811 2020).
38. Duan, J., Álvarez-Pérez, G., Voronin, K. V., Prieto, I., Taboada-Gutiérrez, J., Volkov, V. S., Martín-Sánchez, J., Nikitin, A. Y. & Alonso-González, P. Enabling Propagation of Anisotropic Polaritons along Forbidden Directions via a Topological Transition. *Science Advances* **7**, eabf2690. doi:10.1126/sciadv.abf2690 (2021).
39. Álvarez-Pérez, G., Duan, J., Taboada-Gutiérrez, J., Ou, Q., Nikulina, E., Liu, S., Edgar, J. H., Bao, Q., Giannini, V., Hillenbrand, R., Martín-Sánchez, J., Nikitin, A. Y. & Alonso-González, P. Negative Reflection of Nanoscale-Confined Polaritons in a Low-Loss Natural Medium. *Science Advances* **8**, eabp8486. doi:10.1126/sciadv.abp8486 (2022).
40. Sahoo, N. R., Dixit, S., Singh, A. K., Nam, S. H., Fang, N. X. & Kumar, A. High Temperature Mid-IR Polarizer via Natural In-Plane Hyperbolic Van Der Waals Crystals. *Advanced Optical Materials* **10**, 2101919. doi:10.1002/adom.202101919 (2022).
41. Guo, X., Wu, C., Zhang, S., Hu, D., Zhang, S., Jiang, Q., Dai, X., Duan, Y., Yang, X., Sun, Z., Zhang, S., Xu, H. & Dai, Q. Mid-Infrared Analogue Polaritonic Reversed Cherenkov Radiation

- in Natural Anisotropic Crystals. *Nature Communications* **14**, 2532. doi:10.1038/s41467-023-37923-w (1 2023).
42. Hu, H., Chen, N., Teng, H., Yu, R., Xue, M., Chen, K., Xiao, Y., Qu, Y., Hu, D., Chen, J., Sun, Z. & Li, P. Gate-Tunable Negative Refraction of Mid-Infrared Polaritons. *Science*. doi:10.1126/science.adf1251 (2023).
 43. Sternbach, A. J., Moore, S. L., Rikhter, A., Zhang, S., Jing, R., Shao, Y., Kim, B. S. Y., Xu, S., Liu, S., Edgar, J. H., Rubio, A., Dean, C., Hone, J., Fogler, M. M. & Basov, D. N. Negative Refraction in Hyperbolic Hetero-Bicrystals. *Science*. doi:10.1126/science.adf1065 (2023).
 44. Enders, M. T., Sarkar, M., Giteau, M., Deeva, A., Herzig Sheinfux, H., Shokooh-Saremi, M., Koppens, F. H. L. & Papadakis, G. T. Deeply Sub-wavelength Mid-Infrared Phase Retardation with α -MoO₃ Flakes. *Communications Materials* **5**, 1–7. doi:10.1038/s43246-024-00453-z (2024).
 45. Wu, B.-Y., Shi, Z.-X., Wu, F., Wang, M.-J. & Wu, X.-H. Strong Chirality in Twisted Bilayer α -MoO₃. *Chinese Physics B* **31**, 044101. doi:10.1088/1674-1056/ac3740 (2022).
 46. Hou, S., Hu, H., Liu, Z., Xing, W. & Zhang, J. Broadband Transmissive Polarization Rotator by Gradiently Twisted α -MoO₃. *Applied Physics Letters* **124**, 111107. doi:10.1063/5.0191145 (2024).
 47. Lu, J., Sang, T., Pian, C., Ouyang, S. & Jing, Z. Tailoring Intrinsic Chiroptical Responses via Twisted Bilayer α -MoO₃ Separated by a VO₂ Film. *APL Photonics* **9**, 046112. doi:10.1063/5.0197081 (2024).
 48. Song, D., Wu, B., Liu, Y., Wu, X. & Yu, K. Strong Circular Dichroism with High Quality Factor Enabled by Hyperbolic Material α -MoO₃ in Mid-Infrared Range. *Optics & Laser Technology* **175**, 110735. doi:10.1016/j.optlastec.2024.110735 (2024).
 49. Wang, Y., Wang, M., Wu, B., Liu, H. & Wu, X. Strong Chirality and Asymmetric Transmission Effect in Twisted Bilayer α -MoO₃ in Terahertz Band. *Optics & Laser Technology* **174**, 110581. doi:10.1016/j.optlastec.2024.110581 (2024).
 50. Castellanos-Gomez, A., Buscema, M., Molenaar, R., Singh, V., Janssen, L., Zant, H. S. J. van der & Steele, G. A. Deterministic Transfer of Two-Dimensional Materials by All-Dry Viscoelastic Stamping. *2D Materials* **1**, 011002. doi:10.1088/2053-1583/1/1/011002 (2014).
 51. Sarkar, M., Enders, M. T., Shokooh-Saremi, M., Watanabe, K., Taniguchi, T., Sheinfux, H. H., Koppens, F. H. L. & Papadakis, G. T. *Retrieving Optical Parameters of Emerging van Der Waals Flakes* arXiv: 2305.13994 [physics.optics]. <http://arxiv.org/abs/2305.13994>. Pre-published.
 52. Kilchoer, C., Abdollahi, N., Steiner, U., Gunkel, I. & Wilts, B. D. Determining the Complex Jones Matrix Elements of a Chiral 3D Optical Metamaterial. *APL Photonics* **4**, 126107. doi:10.1063/1.5127169 (2019).
 53. Kirchhoff, G. Ueber Das Verhältniss Zwischen Dem Emissionsvermögen Und Dem Absorptionsvermögen Der Körper Für Wärme Und Licht. *Annalen der Physik* **185**, 275–301. doi:10.1002/andp.18601850205 (1860).
 54. Sabatke, D. S., Descour, M. R., Dereniak, E. L., Sweatt, W. C., Kemme, S. A. & Phipps, G. S. Optimization of retardance for a complete Stokes polarimeter. *Opt. Lett.* **25**, 802–804. doi:10.1364/OL.25.000802 (2000).
 55. Cao, Y., Fatemi, V., Fang, S., Watanabe, K., Taniguchi, T., Kaxiras, E. & Jarillo-Herrero, P. Unconventional Superconductivity in Magic-Angle Graphene Superlattices. *Nature* **556**, 43–50. doi:10.1038/nature26160 (2018).
 56. Duan, J., Capote-Robayna, N., Taboada-Gutiérrez, J., Álvarez-Pérez, G., Prieto, I., Martín-Sánchez, J., Nikitin, A. Y. & Alonso-González, P. Twisted Nano-Optics: Manipulating Light at the Nanoscale with Twisted Phonon Polaritonic Slabs. *Nano Letters* **20**, 5323–5329. doi:10.1021/acs.nanolett.0c01673 (2020).
 57. Di Battista, G., Seifert, P., Watanabe, K., Taniguchi, T., Fong, K. C., Principi, A. & Efetov, D. K. Revealing the Thermal Properties of Superconducting Magic-Angle Twisted Bilayer Graphene. *Nano Letters* **22**, 6465–6470. doi:10.1021/acs.nanolett.1c04512 (2022).